Carbon 174 (2021) 396–403

Contents lists available at ScienceDirect

Carbon

journal homepage: www.elsevier.com/locate/carbon

Research Article

Graphene and graphene oxide on Ir(111) are transparent to wetting but not to icing

Signe Kyrkjebø [a, b], Andrew Cassidy [b], Naureen Akhtar [a, c], Richard Balog [b], Martha Scheffler [b], Liv Hornekær [b], Bodil Holst [a], Ranveig Flatabø [a, *]

[a] University of Bergen, Department of Physics and Technology, Bergen, Norway
[b] Aarhus University, Department of Physics and Astronomy, Aarhus, Denmark
[c] University of Agder, Department of Engineering Sciences, Grimstad, Norway

ARTICLE INFO

Article history:
Received 21 October 2020
Received in revised form
8 December 2020
Accepted 10 December 2020
Available online 17 December 2020

Keywords:
Anti-icing coating
Icephobicity
Wettability
Graphene oxide
Graphene
Iridium

ABSTRACT

Anti-icing coatings reduce the freezing onset temperature for water by changing the chemical and physical environment at the water-substrate interface to prevent ice nucleation and growth. Graphene oxide has several attributes that make it attractive as an anti-icing coating and it has been theoretically predicted that graphene oxide has a lower freezing onset temperature than pristine graphene. Here, we test this hypothesis using carefully prepared, well-characterized graphene oxide substrates. We compare the water contact angle for graphene and graphene oxide coatings, both prepared on iridium(111) surfaces. The results show both materials to be transparent to wetting, but indicate a lower freezing onset temperature for graphene oxide than for pristine graphene. The measured water contact angles are dominated by the properties of the underlying Ir(111) substrate while the freezing onset temperature is dictated by the functional groups present on the graphene basal plane. We suggest that the lowering of the freezing onset temperature is caused by the formation of a viscous water layer on the surface. Scanning tunneling microscopy and x-ray photoelectron spectroscopy data are used to evaluate the robustness of the coating material and suggest ways to improve the long-term performance, namely by advancing strategies to avoid water intercalation.
© 2020 The Author(s). Published by Elsevier Ltd. This is an open access article under the CC BY license (http://creativecommons.org/licenses/by/4.0/).

1. Introduction

Oxygen-functionalized graphene is one of the most common graphene derivatives. Graphene oxide was synthesized for the first time by exposing graphite to strong acids by B. Brody in 1859 [1]. Nowadays, graphene oxide is usually produced by the Hummers' method, see e.g. Ref. 2. It can be made into fibers [2], membranes [3], papers [4] and freestanding multilayered films [5], and it can be drop-casted onto various substrates [6]. Applications range from energy storage [7] and water treatment [8] to sensors for detection of gas and vapor [9] or biosensing [10], and protective coatings [11]. The basal plane of chemically synthesized graphene oxide is mainly covered with hydroxyl- and epoxy groups, see Fig. 1. The edges likely contain carboxyl-, carbonyl- and phenol groups [12]. Graphene oxide is non-stoichiometric with a O:C ratio usually in the range 0.3–0.5 depending on the oxidation conditions during the synthesis [13,14]. The oxygen-containing groups are often distributed in the form of islands that are interspersed with regions of bare graphene [15].

Graphene oxide is hydrophilic, i.e., it is readily dispersible in water, with a reported water contact angle (WCA) in the range of 25°–55° [16–19]. Carboxyl- and hydroxyl groups are considered the main hydrophilic functional groups. By removing the carboxyl groups from graphene oxide using non-thermal microwaves, Rasuli et al. [20] observed an increase in the WCA from ~30° to ~70°. Zhang et al. [18], found that UV irradiation of graphene oxide induced an increase in the WCA from around 28° to around 58°. They attributed this change to the removal of hydroxyl- and carbonyl groups.

The relatively large spread in the observed WCA is typical for graphene-based materials; their wettability is highly debated. Pristine graphene has been suggested to be hydrophilic [21] and hydrophobic [22]; transparent [23] and opaque [24] to wetting. Prydatko et al. [21], recently claimed that free-standing, clean graphene is hydrophilic with a WCA of 42° ± 3°. The same authors

* Corresponding author.
E-mail addresses: Bodil.Holst@uib.no (B. Holst), Ranveig.Flatabo@uib.no (R. Flatabø).

https://doi.org/10.1016/j.carbon.2020.12.030
0008-6223/© 2020 The Author(s). Published by Elsevier Ltd. This is an open access article under the CC BY license (http://creativecommons.org/licenses/by/4.0/).

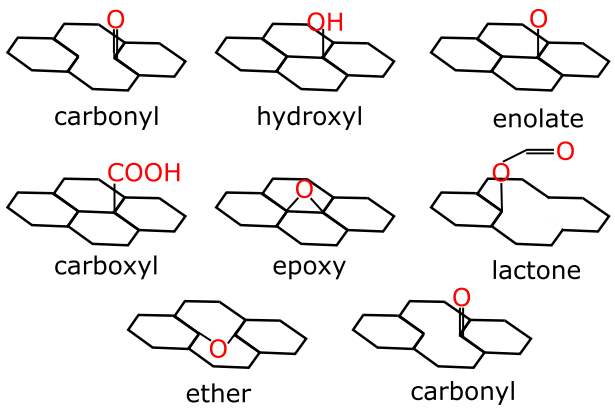

Fig. 1. Various functional groups found in oxygen-functionalized graphene. (A colour version of this figure can be viewed online.)

found the WCA of highly oriented pyrolytic graphite (HOPG) to be 60° ± 3°. In general, the observed WCA of graphene-based materials strongly depends upon the condition of the graphene (referring to quality, storage, cleanliness and chemical functionalization), hydrocarbon contamination from ambient air, the measurement conditions and, when supported by a substrate, the properties of the underlying substrate (including cleanliness, roughness, chemical composition and preparation) [25–27].

Despite its hydrophilic nature, graphene oxide has been predicted to have superior icephobic properties to pristine graphene, i.e., graphene oxide is predicted to better repel ice growth [28–31]. Zokaie et al. [29], calculated the freezing onset temperature for confined water between two graphene oxide sheets to be −37°C. The functional groups were found to force the water molecules near the sheets to remain in a liquid state and this was attributed to confinement effects. The mean ice nucleation temperature of water containing graphene oxide sheets (average sheet size 8 nm or smaller) was experimentally demonstrated to be around −28°C by Bai et al. [31] Geng et al. [30], showed that a graphene oxide dispersion can suppress the growth of ice crystals, and concluded that graphene oxide behaves as an antifreeze protein. Specifically, they found the hydroxyl group on the graphene basal plane to be responsible for the inhibition of the ice growth.

The non-stoichiometric nature of chemically synthesized graphene oxide makes it challenging to control its properties [13]. One way to achieve uniform functionalization or to selectively functionalize one site over another is to expose graphene produced via chemical vapor deposited (CVD) to atomic oxygen. CVD on single crystals can yield high-quality graphene with a low concentration of defects. In particular, graphene growth via low pressure CVD on Ir(111) has been shown to produce highly crystalline graphene sheets with excellent structural coherency [32]. It was widely assumed that epoxy groups are the main functional group on the basal plane of CVD-grown graphene oxide [33,34]. However, enolate functional groups, first predicted based on theoretical calculations of graphene oxide on Cu(111) [35], have recently been reported following oxidation of graphene islands on Ru(0001) [36] and entire graphene sheets on Ir(111) [37]. In these graphene-transition metal systems the enolate bond forms when the oxygen atoms bind to a single carbon atom and the neighboring carbon atoms binds to metal atoms in the underlying substrate (see Fig. 1).

Here we investigate the WCA and freezing onset temperature of enolate-functionalized graphene on Ir(111). The results are compared to pristine graphene on Ir(111). The surfaces are characterized using scanning tunneling microscopy (STM) and x-ray photoelectron spectroscopy (XPS) before and after exposure to air, water droplets and ice.

2. Materials and methods

The growth and characterization via STM and XPS of graphene samples took place in ultra-high vacuum (UHV) chambers with base pressures below 1×10^{-9} mbar at Aarhus University, DK. WCA and freezing-onset temperature measurements were made under bench conditions at the University of Bergen, NO.

Graphene sheets were prepared in UHV on the (111) surface of a 3 mm thick Ir single crystal with a diameter of 7 mm. The iridium surface was cleaned through several sputter cycles using Ne^+ ion bombardment at 1.5 keV followed by annealing in an oxygen atmosphere. The graphene sheet was prepared by temperature programmed growth at 1200°C followed by chemical vapor deposition at 900°C, using ethylene gas as the carbon source [38]. Clean substrates were exposed to ethylene at a background pressure of 3×10^{-7} mbar at room temperature for 15 min. The background gas was pumped away and the sample was annealed to 1200°C briefly before cooling to 900°C. Graphene growth continued at 900°C by again exposing to ethylene at a background pressure of 3×10^{-7} mbar for 15 min. The background gas was removed and samples were cooled to room tempearture at a rate of 0.2°C/s. Graphene samples were exposed to atomic oxygen in a separate UHV chamber. Transfer between chambers were done using a vacuum suitcase with a base pressure of 1×10^{-5} mbar. After transfer, pristine graphene samples were annealed in UHV to 120°C for 20 min, before exposure to the O-atom source at room temperature. Samples were exposed to a flux of O atoms at normal incidence, produced by thermally cracking O_2 in an Ir capillary heated to 1560°C (Oxygen Atom Beam Source, MBE Komponenten GmbH). The cracker was thoroughly degassed prior to use. O_2 gas was backfilled through the capillary into the UHV chamber, to facilitate atomic dosing. In all cases the pressure in the main chamber during exposure to atomic oxygen was fixed at 2×10^{-7} mbar giving an estimated flux of 5×10^{12} atoms cm^{-2} s^{-1} at the sample.

STM images were recorded at room temperature using an Aarhus type STM [39] and all images were collected in constant current mode. Images were analysed using the WsXM software [40] and were corrected for thermal drift and plane flattened. XPS data were recorded using Phobios 100 energy analyzers (Specs, Germany). Low-resolution data were collected in the surface dynamics laboratory, Aarhus, using a Mg anode at 1253.6 eV of an XR50 X-ray source (Specs, Germany) and electrons were collected from the entire crystal surface. High-resolution data were collected at the MatLine end station connected to the ASTRID 2 synchrotron source, Aarhus. At the Matline end station photon energies of 340 eV and 650 eV were used to collect data for C1s and O1s core levels, respectively, from a spot size of a few 100 μm. All XPS data were fitted using the KolXPD software [41].

Freezing onset temperatures and WCA were measured in Bergen using a DataPhysics OCA 20 instrument (DataPhysics GmbH, Germany). The measurements were done in ambient air at room temperature, 22°C ± 2°C, and a relative humidity of 30% ± 2%. Samples were housed in a copper block to ensure good thermal contact between a Peltier cooling plate and the sample, and a K-type thermocouple was used to measure the temperature of the iridium crystal. A 2 μL water droplet of deionized water was placed on the substrate surface at room temperature and the WCA was measured. The sample was then cooled at a rate of 0.16°C/s until the droplet froze. This allowed for measurement of WCA as a function of temperature and for identification of the freezing onset temperature. WCA measurements were conducted over multiple days to check the stability of the substrate to contamination effects.

3. Results and discussion

3.1. Surface characterization of graphene oxide on Ir(111)

Fig. 2 shows STM data recorded for graphene on Ir(111) (Gr/Ir(111)) (a) before and (b) after exposure to a fluence of 1×10^{15} O-atoms cm^{-2}. The slight mismatch between the graphene lattice constant and the Ir(111) surface atoms results in a moiré structure with a repeat periodicity of 2.5 nm ± 0.2 nm, visible in Fig. 2 (a). Each moiré unit cell contains three high symmetry areas: i) ATOP regions where an Ir atom sits directly underneath the center of a carbon hexagon; and ii) HCP and iii) FCC regions, where every second carbon atom is positioned directly above an Ir atom. In FCC regions, the neighboring carbon atom lies above an iridium atom in the second surface layer while in HCP the neighboring carbon atom lies above an Ir atom located in the third layer. The remaining carbon atoms, in between ATOP and FCC/HCP regions, show varying degrees of overlap with the underlying surface Ir atoms [42].

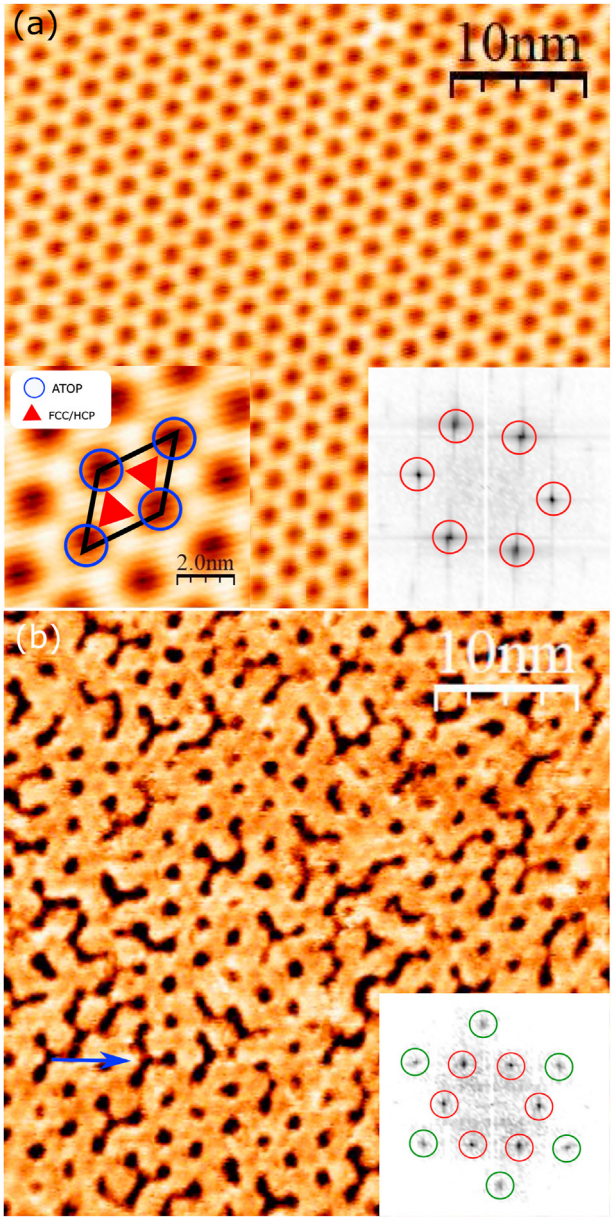

Fig. 2. STM images of (a) Gr/Ir(111) and (b) O-Gr/Ir(111) before wetting and icing experiments. (a) The moiré pattern demonstrates the single-crystal nature of the graphene sheet. The left inset demonstrates the labelling of different areas in the moiré unit cell as ATOP, HCP and FCC. The right inset is the spatial FFT of the image and shows the periodicity of the moiré structure. It: 870.0 pA, Vt: 441.3 mV. (b) After exposure to a fluence of 1×10^{15} O-atoms cm^{-2}, dark circular areas emerge in the STM image, indicating the formation of islands of C–O covalent bonds. The inset shows the FFT of the image, indicating that the islands of graphene oxide follow the moiré pattern. The blue arrow highlights an elongated island of O-functional groups stretching across several moiré unit cells. It: 150.0 pA, Vt: 475.8 mV. (A colour version of this figure can be viewed online.)

It has previously been demonstrated that the moiré pattern in Gr/Ir(111) has an ordering effect on the positioning of O-functional groups when pristine samples are exposed to a fluence of O-atoms [37]. The STM image in Fig. 2(b) concurs with this observation. The dark areas in Fig. 2(b) are ascribed to newly formed O-graphene islands following exposure to O-atoms. The dark areas clearly follow the moiré pattern, with the same lattice constant visible in the image spatial FFT, see inset Fig. 2(b). The inner points in the FFT in Fig. 2(b), red circles, track the moiré unit cells as in Fig. 2(a), while the outer points, offset by 30°, green circles, track the distance between the FCC and HCP areas of each individual moiré unit cell. Cassidy et al. [37], demonstrated that the ordering of O-functional groups is determined by the interaction between the C-atoms in the graphene sheet and the Ir substrate, with O-bonds selectively forming in regions were neighboring carbon atoms can bind down directly to an underlying Ir atom, i.e., at FCC and HCP sites. Studies of H and Ir adatoms on Gr/Ir(111) surfaces, both of which induce similar graphene-metal pinning effect as enolate, show a light preference for bonding at the HCP sites [43,44]. Our data do not allow us to distinguish between the FCC and HCP sites in the moiré unit cell but it is clear in Fig. 2(b) that O-functional groups are predominantly present at one-side of the moiré unit cell and appear as circular islands. Several elongated O-functionalized islands are, however, also observed. An example is highlighted with a blue arrow in Fig. 2(b), indicating that in some areas, O-groups can be bound to both FCC and HCP sites in the same moiré unit cell. The oxidized areas in Fig. 2, that is the dark areas, cover 22% of the surface.

XPS data are shown in Fig. 3 and demonstrate that new functional groups are generated on the graphene basal plane after exposure to atomic oxygen and that these functional groups are predominantly chemically identical to the enolate groups identified by Cassidy et al. [37] Fig. 3(a) shows the binding energy for electrons originating from the O1s core levels for Gr/Ir(111) and O-Gr/Ir(111), while Fig. 3(b) shows the binding energy for electrons originating from the C1s core levels from the same samples. The gray dots show the raw data while the red curves result from fits constructed by fitting different peaks for groups of atoms in different types of chemical environments. O1s data were fitted with Gaussian peaks and C1s data were fitted with Doniach-Šunjić functions convoluted with Gaussian curves. Peak assignments and fitting details can be found in Table S1 and S2 respectively in Suppl. Material.

In the O1s spectra, Fig. 3(a), a nominal intensity of photoelectrons was detected from Gr/Ir(111) before oxidation, with a clear peak emerging after exposure to the O-atom source. Four components were fitted to the spectrum arising from O-Gr/Ir(111): O_1 (533.6 eV), O_2 (532.1 eV), O_3 (531.2 eV), and O_4 (528.8 eV). These peaks can be attributed to O-atoms present in different types of O–C covalent bonds: hydroxyl (O_1), ether (O_2), enolate (O_3) and epoxy- and carbonyl groups (O_4), respectively [15,37,45]. After oxygen exposure, the enolate peak (O_3) is the dominant component, in good agreement with literature [37].

Photoelectrons arising from the C1s core level are shown in Fig. 3(b). The dominant component in the spectrum from Gr/Ir(111) arises from C-atoms in an sp^2-configuration with a binding energy at 284.1 eV (C_4). In Fig. 3(b), C1s photoelectrons are convoluted with

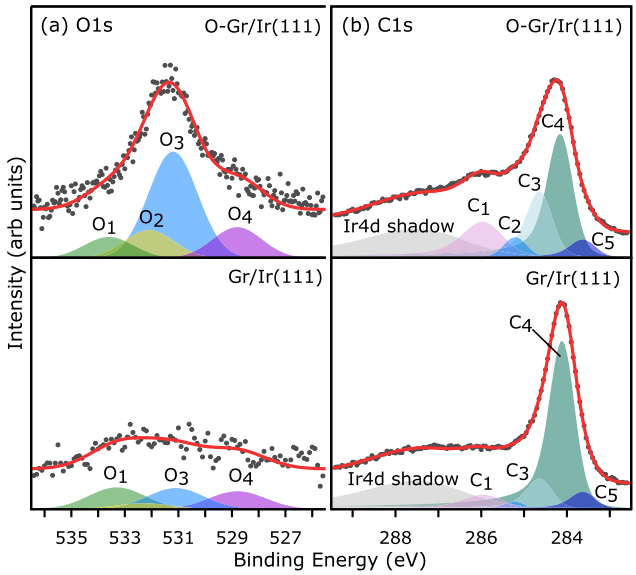

Fig. 3. XPS data from (a) the O1s core level and (b) the C1s core levels from Gr/Ir(111) (bottom panels) and O-Gr/Ir(111) (top panels). Gray dots represent the raw data and the red curve shows a fit resulting from different peaks for atoms in different chemical environments. Peak fitting details can be found in the main text and in Suppl. Material. (A colour version of this figure can be viewed online.)

photoelectrons arising from the Ir4d 5/2 core level, with the position of the latter peak caused by a shadow incident photon beam emitted from the source with an energy of 1242.4 eV. Additional components have been included to fit the data in Fig. 3(b) and are ascribed to carbon atoms in different types of chemical environments, namely C_1 carbonyl groups (285.9 eV), C_2 ether groups (285.3 eV), C_3 enolate groups (284.6 eV) [37,45], and C_5 (283.6 eV) attributed to graphene decoupled from the iridium substrate by intercalated species [46].

The C1s components labelled $C_{1\text{-}3}$ represent the formation of C-atoms in sp^3-configurations and correspond to the formation of C–O covalent bonds. After exposure to atomic oxygen, there is a clear increase in the relative intensity of sp^3 components, however, C_4 is still the dominant component. The fitting indicates that enolate moieties dominate the sp^3-configurations with carbonyl groups also present. This fits with our interpretation of the O1s data in Fig. 3(a). We note that the peak attributed to enolate formation, C_3, corresponds to C-atoms bound to O-atoms and also the neighbouring carbon atoms bound to the underlying Ir-substrate [37]. XPS data in Fig. 3 indicate that the transfer of pristine Gr/Ir(111) samples via the vacuum suitcase led to low-levels of oxidation prior to exposure to the O-atom source. However, the O-Gr/Ir(111) produced via exposure to controlled doses of atomic-O leads to production of predominantly enolate-functionalized graphene, uniformly distributed across the single crystal sheet.

3.2. Wetting and icing experiments

Samples were removed from vacuum and brought to the bench for ice-growth experiments. Images of a sessile water droplet (2 μL) on O-Gr/Ir(111) at various substrate temperatures are presented in Fig. 4. These data show that the O-Gr/Ir(111) surface is almost hydrophobic at room temperature. The WCA is found to be 77° ± 6°, averaged over 32 measurements. This value is significantly higher than values previously reported for water on graphene oxide, where values have typically fallen into a range between 25 and 55° [16–19]. In a separate experiment, the WCA of Gr/Ir(111) was measured at 79° ± 4°, averaged over 32 measurements. Thus, we report that the WCA for Gr/Ir(111) and O-Gr/Ir(111) are the same within errors and it is likely that graphene oxide and pristine graphene on Ir(111) are transparent to wetting. Graphene oxide and bare graphene have different chemical potentials, and if opaque to wetting on Ir(111), the surfaces should exhibit different WCAs. Moreover, the graphene surface is expected to be smooth, dictated by the atomically flat Ir(111) surface. The root mean square roughness, calculated from STM images with a total surface area of 0.2 μm^2, is found to be below 1 nm. Hence, the wettability is mainly dictated by the chemical properties of the substrate and not the surface topography [47]. Göbbels et al. [48], found that the WCA for iridium increases with oxygen content starting at ~82° for bare iridium with a roughness of 1.2 nm, similar to the values reported here.

The WCA measurements for both samples were recorded over several days to check for contamination effects, see Fig. 5(a). We report no significant variation in the measured WCA as a function of time. The fact that the WCA remains relatively constant over a period of several days indicates the stability of both substrates to cycling and a low degree of contamination during experiments.

Fig. 5(b) presents WCA measurements for a water droplet on O-Gr/Ir(111) as a function of the temperature of the iridium crystal. As the temperature decreases so does the WCA. For temperatures above 0°C this is due to condensation, and at sub-zero temperatures frost can facilitate wetting [49]. The large variations in WCA in Fig. 5(b) at around −20°C result from the sudden change in droplet appearance when it freezes. The freezing onset is assumed to mark the start of the freezing process. The droplet heats up adiabatically resulting in a mixed liquid/ice phase. This is evident as a loss of water clarity [50,51]. In the second stage of freezing, the ice front moves upwards and forms a pointy-tip-shaped ice droplet, Fig. 4(c). At this point, heat is released to the substrate by conduction.

The freezing onset temperature is found to be −21°C ± 1°C for O-Gr/Ir(111), averaged over 26 measurements done over five days. It shows no significant variation between measurements done on different days. In comparision, the freezing onset temperature of bare Gr/Ir(111) is found to be −15°C ± 3°C, averaged over 32 experimental runs. The freezing onset temperature for water on O-Gr/Ir(111) reported here is close to that reported elsewhere for water on graphene oxide (sheet size 8 nm) on silicon, down to around −25°C [31], and to that of water on fluorinated graphene on Ru(0001) on sapphire [51], where Akhtar et al. [51], reported a freezing onset temperature of −23°C ± 1°C (estimated 25% fluorine coverage on graphene on Ru(0001) on sapphire), −20°C ± 1°C (estimated 10% fluorine coverage on graphene on Ru(0001) on sapphire) and −18°C ± 1°C (graphene on Ru(0001) on sapphire). Our results indicate that the highly patterned, oxygen-functionalized graphene layer on Ir(111) lowers the freezing onset temperature relative to the freezing onset temperature for water on pristine graphene on Ir(111). A recent theoretical study by Zhang et al. [52], used molecular dynamics simulations to show that functionalization of graphene with Na^+-, Cl^--ions, and methane, lowers the freezing onset temperature via the formation of a viscous water layer on the surface. Since our data indicate the graphene layer to be transparent to wetting, we propose that the oxygen-functional groups behave in a similar fashion to the ion- and methane-functionalization considered by Zhang et al., to reduce the water freezing onset temperature. This also ties in with recent research which suggests that the hydrophobicity of a surface does not determine its icephobic properties, but that the icephobic properties are dominated by surface topography [53].

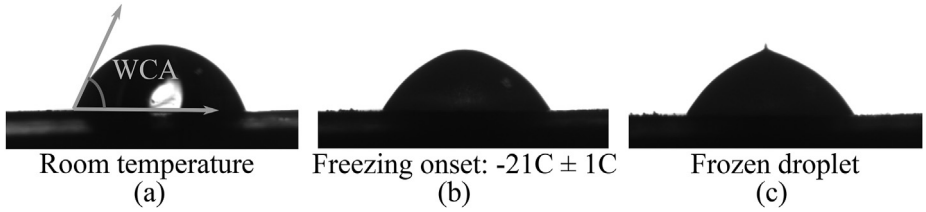

Fig. 4. Snapshots of a sessile water droplet (2 μL) on O-Gr/Ir(111) (a) at room temperature, (b) at the freezing onset where the doplet turns opaque and (c) the frozen state with the characteristic pointy-tip shape.

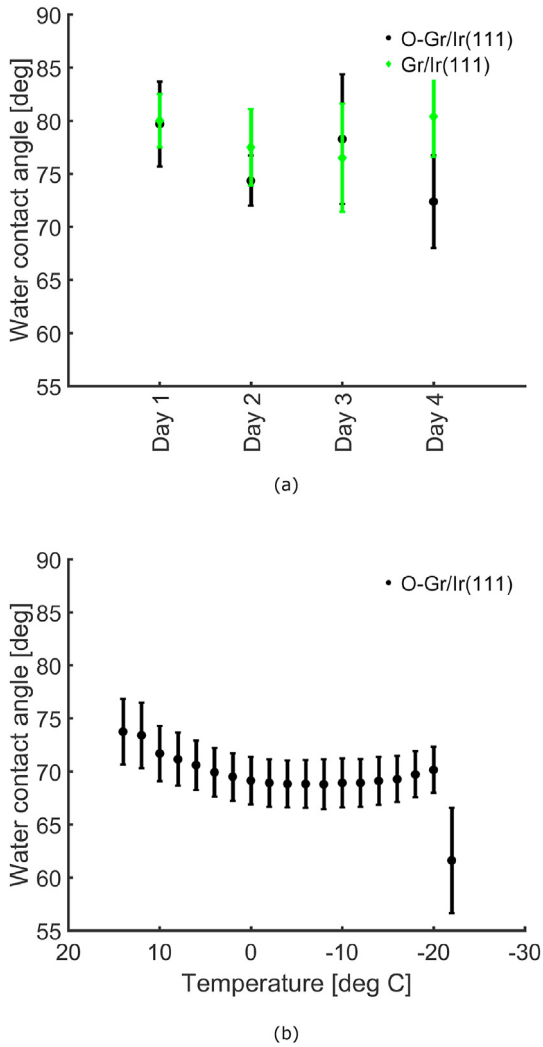

Fig. 5. (a) WCA of a water droplet on O-Gr/Ir(111) (black dots) and Gr/Ir(111) (green diamonds). Each point is the average of eight measurements recorded on the same day. The data show no significant variation as a function of time, indicating that accumulation of dust or other hydrocarbon contaminants does affect the observed WCA. (b) Average WCA of a water droplet on O-Gr/Ir(111) measured as a function of the temperature of the Ir crystal. The plot is the average of eight measurements taken in one day. A sudden change in the WCA is observed at the freezing onset at −21°C ± 1°C, where the droplet changes apperance and becomes opaque. (A colour version of this figure can be viewed online.)

3.3. Surface characterization after exposure to water ice

STM images of both the Gr/Ir(111) and O-Gr/Ir(111) samples obtained after the wetting and icing experiments are presented in Fig. 6. The data indicate that in all cases the graphene layer remains intact after exposure to water and ice but the samples now show heterogeneity. In Fig. 6(a) an STM image of Gr/Ir(111) is displayed. The persistence of the graphene layer is evident from the moiré pattern visible throughout the image. Bright elevated islands are visible at the center of the image. A height profile drawn across the image reveals a height difference of ~1.5 Å between the graphene basal plane and the elevated areas. This height difference is in good agreement with reported values for the height difference induced by water islands intercalated beneath graphene on a metal substrate [54]. Around the islands, dark spots that were not visible in STM images prior to the wetting and ice experiments are observed. Thus, the dark spots are thought to represent the formation of newly reacted centers on the graphene basal-plane, i.e., new reaction sites induced by exposure to air, water, and/or freezing.

Fig. 6(b) and (c) contrast two different types of area on the O-Gr/Ir(111) substrate after exposure to water and ice. The STM image in Fig. 6(b) is very similar to that in Fig. 2(b) representing O-Gr/Ir(111) before WCA measurements; O-functionalized areas appear slightly darker in the image and closely follow the Gr/Ir(111) moiré pattern, with the moiré lattice constant of 2.53 nm ± 0.03 nm. Thus, this area on the surface remains highly oxidized after the wetting and icing experiments. Dark spots in Fig. 6(b) are similar to those described for Fig. 6(a).

In contrast, an STM image of a different type of area on the same surface is presented in Fig. 6(c). In this area, bright elevated islands similar to those seen in Fig. 6(a) are distributed throughout the image. Further elevated white spots appear periodically atop these islands. A height profile, following the blue line across the large island and smaller white spots in Fig. 6(c), is given as the inset and shows a height difference of 1–1.5 Å between the graphene basal plane and the elevated areas, and the same difference between the islands and the white spots. Feng et al. [54], report that water intercalates graphene sheets through grain boundaries on Ru(0001) if the substrate is exposed to water vapor under ultra-high vacuum conditions at temperatures around −163°C. The authors report that water is not uniformly distributed underneath graphene [54], indicating that intercalation is diffusion limited on that substrate. We thus propose that the elevated islands visible in Fig. 6(a) and (c) indicate intercalation of water between the graphene sheets and the Ir substrate, and that the white dot-like structures observed atop these islands in Fig. 6(c) represent the growth of a second layer of water on this sample. The dark spots visible in Fig. 6(c) correspond to the same types of covalently functionalized areas as described in relation to Fig. 6(a).

An atomically-resolved STM image of the area inside the black rectangle in Fig. 6(c) is shown in Fig. 6(d) with the FFT as the inset. This image reveals a hexagonal pattern of atoms with a lattice constant corresponding to that of graphene, confirming that a continuous layer of graphene remains across the area of the elevated regions. The observation of the clean graphene areas atop the elevated islands implies that oxygen-functional groups have been removed from the graphene basal plane following the wetting and icing measurements. Intercalation is only observed in regions where the functional groups have been lost. Fig. 6 shows that the

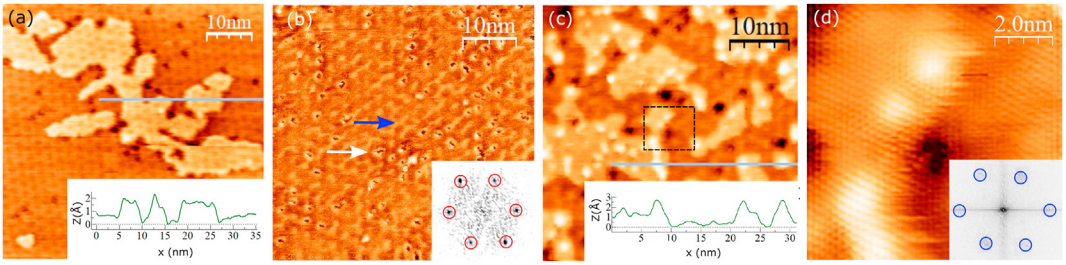

Fig. 6. STM images from (a) Gr/Ir(111) and (b,c,d) O-Gr/Ir(111) obtained after completion of the wetting and icing experiments. (a) The blue line corresponds to the height profile in the inset, 640.0 pA, Vt: 102.2 mV. (b) The blue arrow highlights an example of bright elongated structures proposed to be bare graphene, while the white arrow highlights an example of a reaction site. The inset shows a spatial FFT, It: 440.0 pA, Vt: 38.8 mV. (c) A different area of the O-Gr/Ir(111) sample. The height profile of the blue line is shown as the inset, It: 470.0 pA, Vt: 38.8 mV. (d) An atomically resolved image of bare graphene obtained from the area marked with black rectangle in (b). The inset shows a spatial FFT, It: 440.0 pA, Vt: 38.8 mV. (A colour version of this figure can be viewed online.)

chemical environment is not uniform across the surface after the wetting and icing experiments.

XPS data from O-Gr/Ir(111) samples following wetting and icing experiments are presented in Fig. 7. The gray dots are the raw data and the red curve is the fit. Associated peaks and fitting details can be found in Table S3 and S4 respectively in Suppl. Material. Note that data in Fig. 7 were collected at the MatLine end station at the ASTRID2 synchrotron source resulting in a more surface-sensitve measurement, from a smaller sample region than data presented in Fig. 3. XPS data presented here were collected on the same area of the sample where ice droplets were grown for WCA measurements.

In the O1s spectrum Fig. 7(a), four components were used to fit the data. Three components represent the formation of covalent C–O bonds as in Fig. 3(a): a hydroxyl component (O_1 at 533.6 eV), an ether component (O_2 at 532.1 eV) and an enolate component (O_3 at 531.2). A new peak was introduced as O_{Ir} at 530.0 eV and represents oxygen species interacting with Ir(111), i.e., intercalated oxygen species [46]. The ether component, O_2, dominates the spectrum.

The C1s spectrum, Fig. 7(b) was fitted with the same 5 components used to fit Fig. 3(a). The majority of the intensity has shifted to higher binding energies, when compared to Fig. 3(a), indicating a shift from predominantly sp^2 carbon to predominantly sp^3 carbon. This fits with the STM data in Fig. 6 which illustrated the formation of new reaction sites after ice-exposure. The XPS data here indicate that these new bonds take the form of ethers or enolates, in agreement with the O1s data. Additionally, the C_5 component, ascribed to intercalated graphene regions, is now comparible in size

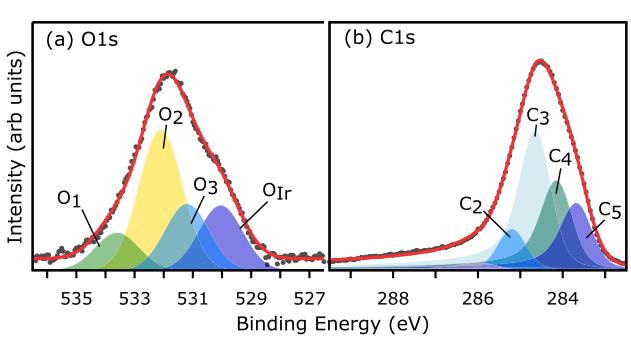

Fig. 7. XPS data from O-Gr/Ir(111) after WCA measurements at the (a) O1s core level and (b) the C1s core level. Data were recorded at the MatLine beamline. The gray dots are the raw data and the red curve represents a fit produced by modelling different types of functional groups in both data sets. Peak details can be found in the text. (A colour version of this figure can be viewed online.)

to the C_4 peak, the latter representing areas of pristine graphene. This indicates significant intercalation after air exposure and WCA measurements [46]. We note that XPS data from Gr/Ir(111) after icing measurements show similar C_5 and O_{Ir} peaks (Fig. S2 in Suppl. Material).

An alternative hypothesis to explain the preponderance of sp^3 carbon in the XPS data shown in Fig. 7(b) is that the XPS sampling area included dust particles or other hydrocarbon contaminants that remained on top of the substrate after WCA measurements. Samples were not annealed prior to these measurements. While it is possible that contaminants contribute towards the large sp^3 carbon, such contaminants were not observed in STM imaging and contamination was not perceived to interfere with contact angle measurements described in relation to Fig. 5. We note that airborne hydrocarbons have been reported to make pristine graphene hydrophobic [55].

Our experiments indicate that a significant amount of intercalation occurs after air exposure. Possible intercalation routes are reported to be through grain boundaries and/or graphene edges [54,56]. The intercalation observed for the O-Gr/Ir(111) sample occurs only in specific regions and leads to the removal of O-functional groups in these regions. Simultaneously, those areas that remain functionalized and avoid intercalation appear to gain more oxygen functional groups, i.e., the density of functional groups in these regions increases. Multiple measurements of water contact angles and freezing onset temperatures were made over several days and these did not indicate any deterioration in the performance of graphene oxide as an anti-icing material over that time period. Hence we conclude that the remaining functionalized regions appear to be sufficient to make the O-Gr/Ir(111) surface more anti-icing then the unfunctionalized Gr/Ir(111) surface. Our data suggest that water intercalation is a kinetically-controlled process and as such it is likely that the patterned formation of enolate functional groups which leads to the simultaneous production of C–Ir bonds plays a role in controlling the extent of intercalation. Future work should consider how pinning the graphene sheet to the Ir surface through covalent bond formation might influence the degree of intercalataion and perhaps prolong the effectiveness of the anti-icing coating. Similar pinning ideas have been persued to prevent CO intercalation beneath H-Gr/Ir(111) [57].

4. Summary

Oxygen-functionalized graphene on Ir(111) was demonstrated to show a lower freezing onset temperature, −21°C ± 1°C, than pristine graphene on Ir(111), −15°C ± 3°C. Both substrates were observed to be almost hydrophobic at room temperature with average WCA of 77° ± 6° for O-Gr/Ir(111) and 79° ± 4° for Gr/Ir(111).

These data suggest that O-Gr and Gr on Ir(111) are transparent to wetting and the values are thought to represent the wetting behavior of the underlying Ir(111) substrate. STM and XPS data demonstrate that the chemical environment of the surface changes after water contact angle measurements and we observe an increase in the number of defects present on the surface as well as intercalation of water and/or oxygen at the graphene-Ir interface. Future research will explore ways to reduce the susceptibility to intercalation.

CRediT authorship contribution statement

Signe Kyrkjebø: wrote the manuscript with support from all authors, Formal analysis, Data analyses were performed, carried out the experiment in collaboration with. **Andrew Cassidy:** carried out the experiment, Formal analysis, Data analyses were performed, wrote the manuscript with support from all authors. **Naureen Akhtar:** conceived the original idea. **Richard Balog:** Formal analysis, Data analyses were performed. **Martha Scheffler:** carried out the experiment. in. **Liv Hornekær:** and B. Holst's laboratory, Formal analysis, Data analyses were performed. **Bodil Holst:** conceived the original idea, Formal analysis, Data analyses were performed. **Ranveig Flatabø:** carried out the experiment, Formal analysis, Data analyses were performed, wrote the manuscript with support from all authors.

Declaration of competing interest

The authors declare that they have no known competing financial interests or personal relationships that could have appeared to influence the work reported in this paper.

Acknowledgment

We acknowledge financial support from The European Research Council (CoG GRANN grant no. 648551). R.F is funded by Norwegian Research Council's FORNY programme's commercialisation project (project number 295961). We thank Zheshen Lee and the ISA team at ASTRID2, DK for help collecting high resolution x-ray photoelectron spectrosopcy data.

Appendix A. Supplementary data

Supplementary data to this article can be found online at https://doi.org/10.1016/j.carbon.2020.12.030.

References

[1] A. Geim, Graphene prehistory, Phys. Scripta 2012 (2012), 014003.
[2] Z. Xu, H. Sun, X. Zhao, C. Gao, Ultrastrong fibers assembled from giant graphene oxide sheets, Adv. Mater. 25 (2013) 188–193.
[3] R. Joshi, S. Alwarappan, M. Yoshimura, V. Sahajwalla, Y. Nishina, Graphene oxide: the new membrane material, Applied Materials Today 1 (2015) 1–12.
[4] D.A. Dikin, S. Stankovich, E.J. Zimney, R.D. Piner, G.H. Dommett, G. Evmenenko, S.T. Nguyen, R.S. Ruoff, Preparation and characterization of graphene oxide paper, Nature 448 (2007) 457–460.
[5] R.K. Upadhyay, S. Naicker, A. Barman, S.S. Roy, T. Thundat, P.R. Waghmare, Fabrication of free-standing graphene oxide films using a facile approach toluene swollen paraffin peeling and green reduction of these films into highly conductive reduced graphene oxide films, Chem. Eng. J. 354 (2018) 149–161.
[6] S. Schöche, N. Hong, M. Khorasaninejad, A. Ambrosio, E. Orabona, P. Maddalena, F. Capasso, Optical properties of graphene oxide and reduced graphene oxide determined by spectroscopic ellipsometry, Appl. Surf. Sci. 421 (2017) 778–782.
[7] F. Li, X. Jiang, J. Zhao, S. Zhang, Graphene oxide: a promising nanomaterial for energy and environmental applications, Nanomater. Energy 16 (2015) 488–515.
[8] Y. Wei, Y. Zhang, X. Gao, Z. Ma, X. Wang, C. Gao, Multilayered graphene oxide membranes for water treatment: a review, Carbon 139 (2018) 964–981.
[9] S. Basu, P. Bhattacharyya, Recent developments on graphene and graphene oxide based solid state gas sensors, Sensor. Actuator. B Chem. 173 (2012) 1–21.
[10] Y. Liu, D. Yu, C. Zeng, Z. Miao, L. Dai, Biocompatible graphene oxide-based glucose biosensors, Langmuir 26 (2010) 6158–6160.
[11] M.J. Nine, M.A. Cole, D.N. Tran, D. Losic, Graphene: a multipurpose material for protective coatings, J. Mater. Chem. 3 (2015) 12580–12602.
[12] D.R. Dreyer, S. Park, C.W. Bielawski, R.S. Ruoff, The chemistry of graphene oxide, Chem. Soc. Rev. 39 (2010) 228–240.
[13] S. Zhou, A. Bongiorno, Origin of the chemical and kinetic stability of graphene oxide, Sci. Rep. 3 (2013) 1–7.
[14] A. Buchsteiner, A. Lerf, J. Pieper, Water dynamics in graphite oxide investigated with neutron scattering, J. Phys. Chem. B 110 (2006) 22328–22338.
[15] D.S. Shin, et al., Distribution of oxygen functional groups of graphene oxide obtained from low-temperature atomic layer deposition of titanium oxide, RSC Adv. 7 (2017) 13979–13984.
[16] N. Wei, C. Lv, Z. Xu, Wetting of graphene oxide: a molecular dynamics study, Langmuir 30 (2014) 3572–3578.
[17] P. Sun, M. Zhu, K. Wang, M. Zhong, J. Wei, D. Wu, Z. Xu, H. Zhu, Selective ion penetration of graphene oxide membranes, ACS Nano 7 (2013) 428–437.
[18] X. Zhang, P. Song, X. Cui, Photoinduced hydrophobic surface of graphene oxide thin films, Thin Solid Films 520 (2012) 3539–3543.
[19] C.-T. Hsieh, W.-Y. Chen, Water/oil repellency and work of adhesion of liquid droplets on graphene oxide and graphene surfaces, Surf. Coating. Technol. 205 (2011) 4554–4561.
[20] R. Rasuli, Z. Mokarian, R. Karimi, H. Shabanzadeh, Y. Abedini, Wettability modification of graphene oxide by removal of carboxyl functional groups using non-thermal effects of microwave, Thin Solid Films 589 (2015) 364–368.
[21] A.V. Prydatko, L.A. Belyaeva, L. Jiang, L. Lima, G.F. Schneider, Contact angle measurement of free-standing square-millimeter single-layer graphene, Nat. Commun. 9 (2018) 1–7.
[22] F. Taherian, V. Marcon, N.F. van der Vegt, F. Leroy, What is the contact angle of water on graphene? Langmuir 29 (2013) 1457–1465.
[23] J. Rafiee, X. Mi, H. Gullapalli, A.V. Thomas, F. Yavari, Y. Shi, P.M. Ajayan, N.A. Koratkar, Wetting transparency of graphene, Nat. Mater. 11 (2012) 217–222.
[24] R. Raj, S.C. Maroo, E.N. Wang, Wettability of graphene, Nano Lett. 13 (2013) 1509–1515.
[25] L.A. Belyaeva, G.F. Schneider, Wettability of graphene, Surf. Sci. Rep. 75 (2020) 100482.
[26] D. Parobek, H. Liu, Wettability of graphene, 2D Mater. 2 (2015), 032001.
[27] D. Ghoshal, R. Jain, N.A. Koratkar, "Graphene's partial transparency to van der waals and electrostatic interactions, Langmuir 35 (2019) 12306–12316.
[28] Y. Zheng, C. Su, J. Lu, K.P. Loh, Room-temperature ice growth on graphite seeded by nano-graphene oxide, Angew. Chem. Int. Ed. 52 (2013) 8708–8712.
[29] M. Zokaie, M. Foroutan, "Confinement effects of graphene oxide nanosheets on liquid–solid phase transition of water, RSC Adv. 5 (2015) 97446–97457.
[30] H. Geng, X. Liu, G. Shi, G. Bai, J. Ma, J. Chen, Z. Wu, Y. Song, H. Fang, J. Wang, Graphene oxide restricts growth and recrystallization of ice crystals, Angew. Chem. Int. Ed. 56 (2017) 997–1001.
[31] G. Bai, D. Gao, Z. Liu, X. Zhou, J. Wang, Probing the critical nucleus size for ice formation with graphene oxide nanosheets, Nature 576 (2019) 437–441.
[32] A.T. N'Diaye, J. Coraux, T.N. Plasa, C. Busse, T. Michely, Structure of epitaxial graphene on Ir(111), New J. Phys. 10 (2008), 043033.
[33] N.A. Vinogradov, K. Schulte, M.L. Ng, A. Mikkelsen, E. Lundgren, N. Mårtensson, A. Preobrajenski, Impact of atomic oxygen on the structure of graphene formed on Ir(111) and Pt(111), J. Phys. Chem. C 115 (2011) 9568–9577.
[34] M.Z. Hossain, et al., Chemically homogeneous and thermally reversible oxidation of epitaxial graphene, Nat. Chem. 4 (2012) 305–309.
[35] J. Jung, H. Lim, J. Oh, Y. Kim, Functionalization of graphene grown on metal substrate with atomic oxygen: enolate vs epoxide, J. Am. Chem. Soc. 136 (2014) 8528–8531.
[36] Z. Novotny, M.-T. Nguyen, F.P. Netzer, V.-A. Glezakou, R. Rousseau, Z. Dohnalek, Formation of supported graphene oxide: evidence for enolate species, J. Am. Chem. Soc. 140 (2018) 5102–5109.
[37] A. Cassidy, S. Pedersen, H. Bluhm, V. Calisti, T. Angot, E. Salomon, R. Bisson, L. Hornekæ r, Patterned formation of enolate functional groups on the graphene basal plane, Phys. Chem. Chem. Phys. 20 (2018) 28370–28374.
[38] J. Coraux, et al., Growth of graphene on Ir(111), New J. Phys. 11 (2009), 023006.
[39] E. Lægsgaard, F. Besenbacher, K. Mortensen, I. Stensgaard, "A fully automated,'thimble-size'scanning tunnelling microscope, J. Microsc. 152 (1988) 663–669.
[40] I. Horcas, R. Fernández, J. Gomez-Rodriguez, J. Colchero, J. Gómez-Herrero, A. Baro, Wsxm: a software for scanning probe microscopy and a tool for nanotechnology, Rev. Sci. Instrum. 78 (2007), 013705.
[41] https://www.kolibrik.net/en/kolxpd, "Kolxpd: Spectroscopy data measurement and processing," Accessed: June 10 2020.
[42] T.A. N'Diauye, J. Coraux, N.T. Plasa, C. Busse, T. Michely, Structure of epitaxial graphene on Ir(111), New J. Phys. 10 (2008), 043033.
[43] P.J. Feibelman, Pinning of graphene to Ir(111) by flat Ir dots, Phys. Rev. B 77 (2008) 165419.
[44] J.H. Jørgensen, et al., Symmetry-driven band gap engineering in hydrogen functionalized graphene, ACS Nano 10 (2016) 10798–10807.

[45] R. Larciprete, S. Fabris, T. Sun, P. Lacovig, A. Baraldi, S. Lizzit, Dual path mechanism in the thermal reduction of graphene oxide, J. Am. Chem. Soc. 133 (2011) 17315–17321.
[46] E. Grånäs, et al., Oxygen intercalation under graphene on Ir(111): energetics, kinetics, and the role of graphene edges, ACS Nano 6 (2012) 9951–9963.
[47] N. Giovambattista, P.G. Debenedetti, P.J. Rossky, Effect of surface polarity on water contact angle and interfacial hydration structure, J. Phys. Chem. B 111 (2007) 9581–9587.
[48] K. Göbbels, T. Kuenzel, A. van Ooyen, W. Baumgartner, U. Schnakenberg, P. Bräunig, Neuronal cell growth on iridium oxide, Biomaterials 31 (2010) 1055–1067.
[49] G. Heydari, E. Thormann, M. Jarn, E. Tyrode, P.M. Claesson, Hydrophobic surfaces: topography effects on wetting by supercooled water and freezing delay, J. Phys. Chem. C 117 (2013) 21752–21762.
[50] S. Jung, M. Dorrestijn, D. Raps, A. Das, C.M. Megaridis, D. Poulikakos, Are superhydrophobic surfaces best for icephobicity? Langmuir 27 (2011) 3059–3066.
[51] N. Akhtar, G. Anemone, D. Farias, B. Holst, Fluorinated graphene provides long lasting ice inhibition in high humidity, Carbon 141 (2019) 451–456.
[52] X.-X. Zhang, M. Chen, Icephobicity of functionalized graphene surfaces, J. Nanomater. 2016 (2016).
[53] P. Eberle, M.K. Tiwari, T. Maitra, D. Poulikakos, Rational nanostructuring of surfaces for extraordinary icephobicity, Nanoscale 6 (2014) 4874–4881.
[54] X. Feng, S. Maier, M. Salmeron, Water splits epitaxial graphene and intercalates, J. Am. Chem. Soc. 134 (2012) 5662–5668.
[55] Z. Li, et al., Effect of airborne contaminants on the wettability of supported graphene and graphite, Nat. Mater. 12 (2013) 925–931.
[56] G. He, Q. Wang, H.K. Yu, D. Farías, Y. Liu, A. Politano, Water-induced hydrogenation of graphene/metal interfaces at room temperature: insights on water intercalation and identification of sites for water splitting, Nano Research 12 (2019) 3101–3108.
[57] L. Kyhl, et al., Enhancing graphene protective coatings by hydrogen-induced chemical bond formation, ACS Applied Nano Materials 1 (2018) 4509–4515.